npj Science of Food

https://doi.org/10.1038/s41538-026-00813-8

Article in Press

Valorizing common pomelo peel by-product via a multi-dimensional framework: a functionally equivalent alternative to a rare botanical for liver health

Received: 27 January 2026

Accepted: 16 March 2026

Cite this article as: Liu, Y., Sun, M., Lian, Q. *et al.* Valorizing common pomelo peel by-product via a multi-dimensional framework: a functionally equivalent alternative to a rare botanical for liver health. *npj Sci Food* (2026). https://doi.org/10.1038/s41538-026-00813-8

Yuliang Liu, Mengmeng Sun, Qizhong Lian, Jianan Wang, Xianghe Meng, Davron Dekhkonov, Hilola Ahunova, Komiljon Tojibaev, Min He & Dong Li

Valorizing Common Pomelo Peel By-product via a Multi-Dimensional Framework: A Functionally Equivalent Alternative to a Rare Botanical for Liver Health

Yuliang Liu[a,c,†], Mengmeng Sun[a,c,†,*], Qizhong Lian[a,c], Jianan Wang[a,c], Xianghe Meng[c,d], Davron Dekhkonov[e], Hilola Ahunova[f], Komiljon Tojibaev[f], Min He[a,c,*], Dong Li[b,*].

[a]*Northeast Research Asia Institute of Traditional Chinese Medicine, Changchun University of Chinese Medicine, Jingyue Economic Development District, Changchun 130117, China;*

[b]*Central Laboratory, Dongguan Hospital of Guangzhou University of Chinese Medicine, Dongguan, Guangdong 523005, China;*

[c]*The Jilin Province School-Enterprise Cooperation Technology Innovation Laboratory of Herbal Efficacy Evaluation Based on Zebrafish Model Organisms, Changchun University of Chinese Medicine, Jingyue Economic Development District, Changchun 130117, China;*

[d]*Wish Technology, Building E11, Area B, Beihu Science and Technology Park, High-tech North District, Changchun 130102, China;*

[e]*Namangan State University, Bobur shox str., 161, Namangan, 60107161, Uzbekistan;*

[f] *Institute of Botany, Academy of Sciences of Uzbekistan, 100125, Tashkent, Uzbekistan.*

[†] These authors contributed equally to this work.

***Corresponding Authors at:**

Central Laboratory, Dongguan Hospital of Guangzhou University of Chinese Medicine, Dongguan, Guangdong 523005, China.

Changchun University of Chinese Medicine, No. 1035, Boshuo Rd, Jingyue Economic Development District, Changchun 130117, China.

E-mail addresses: sunmm@ccucm.edu.cn (M. Sun); hemin@ccucm.edu.cn (M. He); lidong.0107@163.com (D. Li)

Abstract

Turning agricultural and food processing by-products into health-promoting ingredients is pivotal for developing sustainable food systems. This study developed an integrated multi-dimensional evaluation framework to assess whether the common pomelo peel by-product (*Citrus grandis* (L.) Osbeck, CGO) can serve as a functionally equivalent alternative to the rare *Citrus grandis* 'Tomentosa' (CGT) for functional food ingredient development. The framework combined comparative metabolomics and delayed luminescence profiling to characterize chemical and physical properties, alongside multi-parametric *in vivo* bioactivity and safety assessment in a diet-induced vertebrate model. Analyses confirmed CGO and CGT as distinct chemotypes and physicotypes, with differential enrichment in bioactive pathways like phenylpropanoid biosynthesis. Crucially, both extracts demonstrated statistically equivalent efficacy in alleviating hepatic steatosis, oxidative stress, and inflammation in a high-cholesterol diet-induced zebrafish model, and modulated key genes related to lipid metabolism, antioxidant response, and inflammation. Safety assessment revealed CGO's significantly wider safety margin. Data integration across dimensions demonstrates that despite compositional differences, the net bioactivity converges on similar beneficial outcomes for liver metabolic health. This work provides a validated strategy for transforming underutilized residues into a multi-target, dietary-relevant ingredient, offering a replicable framework for resource-efficient development of sustainable functional crops and food supply chains.

Keywords: Pomelo peel; By-product; Metabolomics; Zebrafish; Liver health; Equivalence; Sustainability

Introduction

The valorization of agricultural and food processing by-products into high-value ingredients is a cornerstone strategy for developing sustainable and circular food systems[1]. Within this paradigm, citrus processing generates substantial waste, with peels accounting for approximately 30-50% of the fruit's fresh weight. Global pomelo (*Citrus grandis*) production has exceeded 9 million metric tons annually in recent years, implying a vast and underutilized stream of peel by-product[2]. These residues are rich in bioactive flavonoids, phenolic acids, and other secondary metabolites, positioning them as promising candidates for functional food ingredient development[2].

Concurrently, metabolic dysfunction-associated steatotic liver disease (MASLD), formerly termed non-alcoholic fatty liver disease (NAFLD), has emerged as a prevalent global health burden, affecting approximately 30% of the adult population[3]. The condition is characterized by hepatic lipid accumulation, oxidative stress, and chronic inflammation[4-6], and currently has limited approved pharmacological therapies. This therapeutic gap has intensified the search for dietary bioactive compounds capable of modulating these interconnected pathological pathways[7,8], creating a compelling opportunity to valorize food by-products for metabolic health applications.

Pomelo peel has attracted particular research interest in this context. The dried peel of *Citrus grandis*, known as "Huajuhong" in traditional Chinese medicine, has been used historically to support digestive and metabolic functions[9]. Recent studies have begun to validate these traditional applications through modern biomedical investigation. Deng et al. demonstrated that *Citrus grandis* 'Tomentosa' (CGT) alleviates MASLD progression by mitigating lipid accumulation and iron metabolism disorders in rodent models[10]. Hu et al. reported that citrus peel powder modulates liver metabolites and gut microbiota composition in mice with diet-induced MASLD[11]. Tian et al. identified coumarin analogues from *Citrus grandis* (L.) Osbeck (CGO) with significant hepatoprotective activity[12]. Most recently, Li et al. showed that CGT ameliorates alcoholic liver disease through regulation of hepatic lipid metabolism and iron homeostasis[13]. Collectively, these studies establish a robust preclinical evidence base supporting the potential of pomelo peel-derived bioactivities in managing liver metabolic disorders.

A pivotal regulatory development has further underscored the practical importance of pomelo peel. In 2024, *Citrus grandis* peel was formally included in China's "Medicinal and Food Homology" directory, unlocking substantial opportunities for its incorporation into functional foods. However, this designation brings a critical supply chain consideration into focus: the Chinese Pharmacopoeia recognizes two botanical origins for this material—the rare CGT and the common CGO[14,15]. CGT is geographically restricted to specific regions of Guangdong Province, with production constrained by limited cultivation areas and specific environmental requirements, rendering it

fundamentally incompatible with the scale required for industrial functional food development[14-17]. Conversely, CGO is widely cultivated throughout southern China and represents an abundant, year-round by-product of the fruit processing industry[1-2].

This disparity between regulatory opportunity and supply reality frames the central question addressed by our study. Can the common, scalable CGO functionally substitute for the rare CGT as a viable source of bioactivity for supporting liver metabolic health? Previous comparative investigations have focused primarily on compositional profiling or generic antioxidant capacity[18,19], leaving a critical gap in application-oriented functional evaluation. Specifically, a direct, multi-parametric comparison in a vertebrate model is lacking to determine their functional equivalence on MASLD-relevant endpoints.

To address this gap, we established an integrated multi-dimensional evaluation framework. First, we comprehensively characterized the chemical profiles of both varieties using comparative metabolomics and assessed their physical states via delayed luminescence (DL)[20]. Subsequently, we conducted a comparative *in vivo* evaluation in a zebrafish model of diet-induced hepatic steatosis, quantifying effects on lipid accumulation, oxidative stress, inflammation, and the expression of key regulatory genes. This study tests the hypothesis that CGO is functionally equivalent to CGT in its capacity to mitigate MASLD-relevant pathologies. By systematically comparing a rare, high-cost material with an abundant by-product across chemical, physical, and biological dimensions—and by applying a normalized analytical framework to directly address compositional differences—our work aims to provide a replicable scientific model for evidence-based substitution decisions in the functional food sector, transforming an underutilized residue into a validated resource for metabolic health applications.

Results and Discussion

Naringin Content of Pomelo Peel Extracts.

As the primary quality marker specified for *Citrus grandis* peel[21], naringin content was quantified in all batches of CGT and CGO extracts by HPLC (Figure 2A). The measured naringin content ranged from 10.00% to 16.40% across all batches, with all values substantially exceeding the Chinese Pharmacopoeia's minimum requirement of 3.5% (Figure 2B). This confirms that all materials used in this study meet the established quality standard for medicinal and food applications.

Comparison between the two botanical origins revealed a significant difference in naringin accumulation. The average naringin content was significantly higher in CGT (14.93%) than in CGO (11.49%). This finding aligns with the traditional perception of CGT as the premium variety

and is consistent with previous reports documenting higher flavonoid accumulation in the rare cultivar[15,16].

Metabolomics Reveals Distinct Chemotypes between CGT and CGO.

A total of 1,835 metabolites were detected, spanning major classes such as flavonoids, lignans and coumarins, and phenolic acids (Figure 3A). PCA of the metabolomics data showed a clear separation between CGT and CGO samples (Figure 3B). The first two principal components (PC1 and PC2) explained 60.02% and 17.24% of the total variance, respectively, indicating that the two botanical origins constitute distinct chemotypes. A comparative heatmap of metabolite class composition further highlighted systematic differences, suggesting that CGT may have higher relative abundances in most metabolite classes, except for alkaloids and steroids (Figure 3C).

Detailed analysis at the individual compound level provided a more nuanced picture (Figure 3D). While distinct, the profiles showed significant overlap, with over 40% of detected metabolites exhibiting higher abundance in CGO. Applying thresholds of |Fold Change| ≥ 0.585 and $p < 0.05$, we identified 575 significantly differential metabolites (Figure 3E). Among these, 292 were upregulated in CGO relative to CGT. The differential metabolites were predominantly from five key classes: flavonoids, lignans and coumarins, alkaloids, phenolic acids, and terpenoids. Notably, while the number of up- and down-regulated flavonoids was balanced, CGO showed a marked reduction in upregulated lignans and coumarins compared to CGT, and an increase in upregulated alkaloids and phenolic acids (Figure 3E). Key differential metabolites within these major compound classes were screened using superimposed FDR ($q < 0.1$) criteria and visually presented via heatmaps (Figure 4).

Our analytical data unequivocally establish that CGT and CGO are fundamentally different entities at the material level. Metabolomics confirmed they are distinct chemotypes**.** While CGT accumulated higher levels of certain compounds like specific flavonoids and lignans and coumarins. CGO presented a rich and unique chemical signature of its own, characterized by substantial abundances of diverse bioactive metabolites, including distinct alkaloid and steroids profiles.

KEGG pathway enrichment analysis of the differential metabolites linked these compositional differences to specific biosynthetic pathways (Figure 5). Significantly enriched pathways included Phenylpropanoid biosynthesis, Flavone and flavonol biosynthesis, and Isoflavonoid biosynthesis. This indicates that the metabolic divergence is not random but rooted in the differential regulation of core biochemical networks responsible for producing bioactive compounds. This not only provides a systems-biology explanation for their divergence into distinct chemotypes but, more

importantly, highlights that these perturbed pathways are the very source of many bioactive molecules, such as naringin.

Consequently, these pathway-level differences are noteworthy precisely because they produce the very compounds implicated in hepatoprotective activity. This raises the central question of our study. Do these compositional and biosynthetic divergences translate into differential efficacy, or do the two extracts converge on similar functional outcomes despite their distinct chemical origins?

Physical Characterization between CGT and CGO by Delayed Luminescence.

Before directly testing those questions in a biological system, we sought to determine whether the chemical differences between CGT and CGO manifest at the physical level. Delayed luminescence (DL) provides a comprehensive and rapid measurement of the global molecular order and energy transfer efficiency within a material[22-25], offering a complementary lens through which to compare the two varieties. If CGT and CGO prove to be not only distinct chemotypes but also distinct "physicotypes," this would further underscore the complexity of their material differences and heighten the interest of whether such divergence nevertheless permits functional equivalence *in vivo*.

Photon emission decay curves showed distinct kinetic profiles between CGT and CGO (Figure 6A). In addition, PCA of the full DL parameters set resulted in clear, separate clustering of CGT and CGO samples (Figure 6B). Moreover, comparative analysis of the derived DL parameters showed systematic differences. CGO samples had greater values for the initial photon intensity (Y_0), the time constant (Tau) and half-life, indicating a slower photon decay, whereas CGT samples displayed a higher decay rate constant (K) and plateau value. This demonstrates that the two varieties possess fundamentally different physical and structural energy states, classifying them as distinct physicotypes (Figure 6C).

These physical differences have practical implications for by-product valorization. The slower photon decay and higher initial intensity observed in CGO suggest a more ordered molecular structure or different energy dissipation pathways, which may influence key processing parameters such as extraction efficiency, powder flowability, and stability during storage[26-28]. From an industrial perspective, such physical characteristics are critical determinants of material handling and downstream formulation, and the distinct physicotype of CGO should be considered alongside its chemical profile when developing standardized functional ingredients from this abundant by-product.

Having established that CGT and CGO differ not only in their chemical composition (chemotypes) but also in their physical energy states (physicotypes), we next asked whether these material-level

divergences translate into differential biological activity. The following sections address this question through *in vivo* safety and efficacy evaluation in a zebrafish model of diet-induced hepatic steatosis.

Safety Assessment Reveals a Wider Safety Margin for CGO.

Prior to efficacy evaluation, we determined the safe concentration ranges of CGT and CGO extracts in zebrafish larvae. Exposure to CGT at 20 μg/mL resulted in about 20% mortality, whereas CGO only reached a similar mortality level at 120 μg/mL (Figure 7A and B). The calculated median lethal concentration (LC_{50}) for CGO (150.1 μg/mL) was approximately 3.5-fold higher than that for CGT (42.6 μg/mL) (Figure 7C and D). This substantial difference indicates a wider safety margin for CGO in this larval model.

The observed disparity in acute toxicity may be attributed to compositional differences between the two extracts. Metabolomic profiling revealed that CGT is significantly enriched in several coumarins and alkaloids (Figure 4), classes of compounds known to exhibit bio-toxic effects in various biological systems[29-31]. For instance, compounds such as bergapten were substantially more abundant in CGT (Figure 4D). While these compounds contribute to the bioactivity of CGT, their higher concentrations may also underlie its narrower safety margin. Conversely, CGO, despite containing lower levels of these specific metabolites, retained a rich profile of other bioactive flavonoids and phenolic acids, which likely contribute to its efficacy without the same level of acute toxicity. This hypothesis warrants further investigation, including targeted toxicity assays of individual compounds, to fully elucidate the toxicological implications of the compositional differences.

From a practical standpoint, the wider safety margin of CGO is a favorable attribute for its development as a food ingredient. It suggests a potentially greater tolerance in processing and formulation, reducing the risk of adverse effects during handling and consumption. Moreover, as an abundant by-product of the citrus industry, CGO offers potential advantages in scalability and supply stability for industrial applications[1,2]. However, direct extrapolation of these larval LC_{50} values to human safety requires caution, as the exposure route (aqueous) differs from oral consumption, and further mammalian toxicity studies are necessary.

Comparative Assessment on Lipid Metabolism and Hepatic Steatosis between CGT and CGO.

Both CGT and CGO extracts effectively attenuated HCD-induced hepatic steatosis in zebrafish larvae, a well-established vertebrate model for assessing MASLD-related pathologies[32,33]. Oil Red O staining revealed severe hepatic lipid accumulation in the HCD model group, which was

markedly attenuated by both CGT and CGO extracts in a dose-dependent manner (Figure 8A). Quantitative image analysis confirmed that medium and high doses of both extracts significantly reduced both the lipid-stained area and intensity (grey value), with effects at the highest doses comparable to the positive control, BZT (Figures 8B, C).

In addition, HCD feeding induced significant elevations in whole-larva total TC and TG. Both extracts effectively modulated these biochemical parameters (Figures 9A, B). A notable difference in the response pattern was observed that CGO demonstrated a consistent, dose-dependent reduction in both TC and TG levels across all tested concentrations. In contrast, CGT significantly lowered TC only at its highest dose and showed a moderating trend for TG at the same concentration.

At the molecular level, RT-PCR analysis of key lipid metabolism genes revealed a highly congruent regulatory pattern between the two extracts (Figure 9C). Both CGT and CGO significantly upregulated the expression of cpt1a (fatty acid oxidation) and downregulated fasn (fatty acid synthesis) and hmgcr (cholesterol synthesis) across multiple dose groups, effectively reversing the HCD-induced dysregulation.

Interestingly, a more robust regulation of hepatic lipid metabolism was observed in the CGO group, as evidenced by its enhanced impact on TC and TG levels. As illustrated in the heatmaps (Figure 4D), CGO is uniquely enriched with bioactive furanocoumarins that are relatively different in CGT. For instance, bergamottin, which is highly abundant in CGO, has been reported to significantly alleviate lipid accumulation by suppressing key adipogenic transcription factors such as PPARγ and C/EBPα[34,35], thereby providing a molecular basis for the enhanced lipid-lowering efficacy observed in the CGO group. Furthermore, the specific accumulation of shikimic acid derivatives, such as 3-O-p-Coumaroyl shikimic acid (Figure 4C), exclusively in the CGO group, provides additional chemical evidence for its specialized role in metabolic regulation[36].

Collectively, these results demonstrate that both CGT and CGO extracts possess substantial and broadly equivalent efficacy in alleviating the core pathological features of MASLD in this model system. They effectively reduce hepatic lipid accumulation, correct systemic dyslipidemia, and restore the expression of pivotal metabolic genes. While the potency of the effect may vary, the principal functional distinction stems from the dose-response characteristics, where CGO exhibits a more consistent and graded effect on key biochemical markers (TC/TG) across the tested concentration range.

Comparative Modulation of Oxidative Stress between CGT and CGO.

Consistent with its role as a key driver of MASLD pathology, pronounced oxidative stress was

evident in HCD-fed larvae[37]. *In vivo* ROS detection using the DCFH-DA probe revealed significantly elevated fluorescence in the hepatic and intestinal regions, which was dose-dependently and significantly attenuated by both CGT and CGO extracts (Figures 10A, B).

Consistent with the ROS findings, HCD feeding led to a marked increase in the lipid peroxidation product malondialdehyde (MDA) and reduced activities of the antioxidant enzymes glutathione peroxidase (GSH-Px) and superoxide dismutase (SOD). Both extracts effectively counteracted these changes in a largely dose-dependent manner (Figures 11A-C). While CGO showed a pronounced effect in reducing MDA levels, CGT appeared to induce a stronger upregulation of GSH-Px and SOD activities at higher doses.

At the transcriptional level, RT-PCR analysis of key genes within the Nrf2/Keap1 antioxidant pathway showed a congruent regulatory pattern (Figure 11D). Both extracts significantly downregulated the expression of nrf2 and its inhibitor keap1 across all doses. For the downstream effector cat, only high-dose CGT and medium-to-high-dose CGO significantly upregulated its expression. Both extracts potently increased the expression of sod1 and gpx1a at high concentrations, with CGT eliciting a particularly strong induction.

The differences in regulatory capacity of CGT compared to CGO might be attributed to the significant enrichment of specific bioactive metabolites as visualized in the heatmaps (Figure 4A). The CGT group exhibits markedly higher levels of key flavonoids, including quercetin, luteolin, and apigenin, which are well-documented to mitigate oxidative stress by activating the Nrf2/Keap1 signaling pathway[38-40]. These compounds serve as potent exogenous antioxidants that upregulate the gene expression of endogenous enzymes such as sod1, cat, and gpx1a, thereby enhancing the activities of SOD and GSH-Px to scavenge ROS. In contrast, the CGO group is characterized by a relative deficiency in these protective compounds, providing a chemical basis for its relatively lower antioxidant efficacy.

These results demonstrate that both CGT and CGO extracts possess largely comparable multi-target efficacy in mitigating HCD-induced oxidative stress. Both extracts effectively reduced ROS overproduction, modulated associated biochemical markers, and restored the expression of core antioxidant genes. Notably, subtle differences in potency for specific endpoints were observed—for instance, CGO showed a pronounced effect on MDA reduction, whereas CGT induced stronger upregulation of GSH-Px and SOD activities at higher doses. These distinct yet effective profiles in re-establishing redox homeostasis reflect the compositional divergence between the two extracts and underscore the complexity of comparing complex mixtures.

Comparative Attenuation of Hepatic Inflammation between CGT and CGO.

Consistent with the central role of chronic inflammation in MASLD progression[41], HCD feeding induced a marked inflammatory response in zebrafish larvae. Using transgenic reporter lines, fluorescence imaging of Tg(mpx:eGFP) and Tg(mpeg:mCherry) larvae revealed substantial infiltration of neutrophils (green) and macrophages (red) into the liver region of the HCD model group, indicating strong diet-induced inflammation (Figures 12A, B). Both CGT and CGO extracts dose-dependently and significantly reduced this immune cell accumulation (Figures 12C, D). Quantitative analysis indicated that CGT exhibited a slightly more potent effect on neutrophil reduction, whereas CGO showed a stronger trend in suppressing macrophage recruitment. In addition, RT-PCR analysis demonstrated that both extracts effectively downregulated the expression of key pro-inflammatory cytokines (Figure 12E). They potently suppressed the expression of tnf-α across all tested doses. While both significantly reduced il-6 expression, CGO showed a more pronounced inhibitory trend.

These findings confirm that both CGT and CGO extracts possess significant efficacy in mitigating HCD-induced hepatic inflammation. They effectively reduce the pathological recruitment of innate immune cells and downregulate central inflammatory mediators. This robust anti-inflammatory activity, combined with their previously demonstrated effects on steatosis and oxidative stress, completes the functional profile of both extracts as multi-target agents against MASLD pathology. The subtle differences in cellular targeting (neutrophils vs. macrophages) further delineate their distinct bioactivity profiles.

Dose-Normalized Analysis Reveals Mechanistic Nuances yet Phenotypic Equivalence between CGO and CGT

The preceding sections demonstrate that both CGT and CGO extracts exert largely comparable multi-target efficacy in alleviating hepatic steatosis, oxidative stress, and inflammation. However, these assessments were based on crude extract concentrations, which do not account for the significant difference in naringin content between the two varieties. To rigorously test whether the observed functional similarities reflect true bio-equivalence—or simply result from compensatory dosing of the less potent extract—we performed a dose-normalized regression analysis, converting all crude extract doses to naringin-equivalent concentrations and examining the dose-response relationships across biochemical, molecular, and phenotypic endpoints.

As shown in Figure 13, the dose-response regression analysis of biochemical and gene expression markers revealed variety-specific mechanistic preferences. CGO exhibited a steeper negative slope in lipid metabolic indicators (e.g., TC, TG, and hmgcr expression) per unit of naringin, indicating a potent direct lipid-lowering capacity despite its lower crude naringin content. This observation

aligns with the more consistent dose-dependent reduction in TC and TG observed for CGO in Figure 9. Conversely, CGT showed a stronger positive slope in upregulating antioxidant enzymes (e.g., SOD, GSH-Px activity, and sod1 expression), suggesting a superior capacity for alleviating oxidative stress per unit of naringin. This is consistent with the stronger induction of GSH-Px and SOD activities by CGT noted in Figure 11.

Despite these mechanistic nuances at the molecular and biochemical levels, the holistic therapeutic outcomes on MASLD phenotypes were remarkably equivalent between CGO and CGT. As visualized in the scatter plots of individual fish (Figure 14), the regression lines for lipid accumulation area, liver grey value, ROS fluorescence intensity, neutrophils and macrophages counts showed extensive overlap in their 95% confidence bands. Furthermore, ANCOVA results (Table 2) confirmed that after adjusting for naringin dosage, there was no statistically significant difference (p>0.05) between CGO and CGT in ameliorating the key pathological phenotypes—hepatic steatosis, ROS levels, and immune cell infiltration.

This apparent paradox—mechanistic divergence at the molecular level converging on phenotypic equivalence—is central to understanding the nature of the functional relationship between CGT and CGO. CGO appears to compensate for its lower total naringin content with higher potency in lipid metabolism regulation per unit of the marker compound. In contrast, CGT relies more heavily on boosting the antioxidant defense system. This phenomenon aligns with the "multi-component, multi-target" principle of natural products, suggesting that the equivalence observed at the phenotypic level is an integrated result of different signaling pathways being modulated to different extents.

Therefore, the significant difference in naringin content between CGT and CGO does not translate into a disparity in their overall efficacy in supporting liver metabolic health. This observation further corroborates our central thesis. For complex botanical extracts, while the content of a single marker compound is an important quality control parameter, the ultimate bioactivity hinges on the collective functional output resulting from the synergistic interaction of multiple constituents. The levels of naringin and other bioactive components present in CGO are entirely sufficient to underpin a biological effect equivalent to that of CGT. Thus, the "equivalence" we claim is not a simple chemical equivalence of naringin content, but a functional bio-equivalence of the whole extract, achieved through distinct yet convergent multi-component synergy.

The validation of this bio-equivalence is particularly significant for the industrial application of CGO. Our results confirm that CGO, a common and abundant food by-product, is not merely a low-quality substitute but a functionally robust ingredient comparable to the rare CGT. By

achieving the same phenotypic recovery through a distinct mechanistic route, CGO represents a sustainable and high-value resource for developing functional foods or anti-MASLD supplements, fully consistent with circular bioeconomy principles.

There are also limitations in this study. The zebrafish model employed in this study, while well-established for multi-parametric *in vivo* screening of metabolic and inflammatory endpoints, has inherent limitations that should be considered when extrapolating the findings. The larvae used (5–11 dpf) have immature hepatic lipid metabolism and immune systems compared to adult vertebrates, and the six-day high-cholesterol diet represents an acute nutritional induction rather than a model of chronic MASLD progression. Similarly, the safety assessment via waterborne exposure reflects larval gill and skin absorption rather than oral ingestion relevant to food use. Therefore, the observed LC_{50} values should be interpreted as comparative toxicological endpoints within this specific model system, but confirmation through mammalian oral toxicity studies remains essential for food safety evaluation.

Despite these caveats, the core finding of functional equivalence between CGO and CGT is robustly supported by the dose-normalized analysis, which accounts for compositional differences and demonstrates phenotypic convergence across multiple endpoints. The observed mechanistic nuances—CGO exhibiting steeper lipid-lowering slopes per unit naringin and CGT showing stronger antioxidant enzyme induction—do not undermine this conclusion; rather, they illustrate how distinct chemical matrices can achieve similar holistic outcomes through different pathways, consistent with the multi-component synergy principle. For the intended application as a sustainable food ingredient, this functional substitutability is the key translational insight. Future studies should extend these findings to mammalian MASLD models with oral administration, include comprehensive toxicological evaluation following food ingredient guidelines, and investigate the bioavailability and stability of the active constituents under relevant processing conditions. Such work will further solidify the evidence base for transforming this abundant by-product into a validated resource for liver health applications.

In conclusion, this study demonstrated that the common pomelo peel by-product CGO is functionally equivalent to the rare CGT in supporting liver metabolic health. The multi-dimensional analysis adopted in the study confirmed that while CGT and CGO are distinct chemotypes and physicotypes, their ethanol extracts elicit statistically indistinguishable efficacy in alleviating hepatic steatosis, oxidative stress, and inflammation in a vertebrate model of diet-induced metabolic dysregulation. From a sourcing perspective, CGO is potentially advantageous due to its abundance as a food by-product, offering scalability and supply stability that the rare CGT cannot provide. These findings showed the common pomelo peel to be a sustainable, high-

potential source for functional food ingredient development. The study also provided a replicable scientific framework for assessing the functional equivalence of alternative botanical resources, offering a pathway to overcome the challenges of scarce traditional materials, enabling the sustainable production of evidence-based functional food ingredients.

Methods

Preparation of Pomelo Peel Samples

Three independent batches of *Citrus grandis* 'Tomentosa' (CGT) peel (Batch Nos. 20240318, 20240608, 20240728) were obtained from Huazhou Lailiyuan Juhong Co., Ltd. (Huazhou, Guangdong, China). Three batches of common *Citrus grandis* (L.) Osbeck (CGO) peel (Batch Nos. 20240101, 20240301, 20240701) were obtained from Guangdong Dongguan Guo Yao Group Co., Ltd. All materials were authenticated by Professor Mengmeng Sun (Changchun University of Chinese Medicine). Voucher specimens were deposited at the Herbarium of Changchun University of Chinese Medicine. The dried peels were pulverized into a fine powder and passed through a 200-mesh sieve prior to extraction.

Extraction and Quantification of Naringin

Extraction: Each batch powder (5.00 g) was accurately weighed and mixed with 100 mL of 80% (v/v) ethanol (solid-to-solvent ratio 1:20, w/v) in a conical flask. After soaking overnight at room temperature, the mixture was subjected to ultrasound-assisted extraction (100 W, 60°C) for 0.5 h[42]. The extract was cooled, filtered, and the residue was re-extracted three more times under identical conditions. All filtrates were combined, concentrated under reduced pressure at 55°C, and lyophilized at -80°C. The resulting ethanol extract powder was stored at 4°C for subsequent analyses.

Naringin quantification: Naringin content was determined by High-Performance Liquid Chromatography (HPLC) following the method specified in the Chinese Pharmacopoeia (2025 Edition)[21]. Analysis was performed on an Agilent 1260 system equipped with an Agilent ZORBAX SB-C18 column (5 μm, 4.6 × 250 mm). The mobile phase consisted of methanol-acetic acid-water (35:4:61, v/v/v) at a flow rate of 1.0 mL/min under isocratic elution. Column temperature was maintained at 40°C, and detection wavelength was set at 283 nm with a 10 μL injection volume. A calibration curve was constructed using a naringin reference standard (Yuanye Bio-Technology, Shanghai, China). Sample extracts were dissolved in methanol, filtered through a 0.22 μm membrane, and analyzed in triplicate. Naringin content was calculated based on peak area and expressed as percentage of dry peel weight.

Metabolomics Profiling

Sample preparation: Freeze-dried peel powder (50 mg) was extracted with 0.5 mL of 70% aqueous methanol at 4°C for 12 h. After centrifugation at 10,000 × g for 5 min, the supernatant was filtered through a 0.22 μm membrane for analysis.

Ultra-performance liquid chromatography-tandem mass spectrometry (UPLC-MS/MS) analysis: Metabolite profiling was performed using an ExionLC™ AD UPLC system coupled with a QTRAP 4500 mass spectrometer (SCIEX). Chromatographic separation was achieved on an Agilent SB-C18 column (1.8 μm, 2.1 × 100 mm) maintained at 40°C. The mobile phase consisted of (A) water with 0.1% formic acid and (B) acetonitrile with 0.1% formic acid, delivered at 0.35 mL/min with the following gradient: 5% B (0 min), increased linearly to 95% B (9 min), held for 1 min, returned to 5% B (11.1 min), and equilibrated until 14 min. Injection volume was 2 μL. Mass spectrometry was conducted with an electrospray ionization source operating in both positive and negative ion modes. The ion spray voltage was set at ±5500 V, source temperature at 550°C, and curtain gas, ion source gas I, and ion source gas II pressures were 25, 50, and 60 psi, respectively. Data acquisition was performed in multiple reaction monitoring (MRM) mode. Metabolite identification was based on matching accurate precursor mass, characteristic MS/MS fragments, and retention time against the MetWare database (MWDB). A quality control sample, prepared by pooling aliquots of all extracts, was injected at regular intervals to monitor system stability[43].

Delayed Luminescence (DL) Measurement

Dried peel samples were ground to particles smaller than 150 μm and equilibrated in a dark desiccator with silica gel at room temperature for at least 16 h. DL measurements were performed using a dedicated system (Meluna Research, Netherlands) as previously described[26]. The setup consisted of a light-tight sample chamber maintained at 22°C and a photomultiplier tube (PMT; 9558QB, Electron Tubes Enterprises Ltd., UK) cooled to -25°C to reduce dark count to ~10 counts/s. For each measurement, 1 g of sample powder was placed in a Petri dish (1 cm diameter). After excitation with white LED light for 10 s, DL emission was recorded at 0.05-s intervals over 60 s, yielding 1200 data points per kinetic curve. Each batch sample was measured in triplicate, with five consecutive readings per replicate, resulting in 15 measurements per batch. The decay curves were fitted to a one-phase exponential decay model in GraphPad Prism 10. The choice of a single-phase model was based on the observation that a mono-exponential fit adequately described the decay ($R^2 > 0.98$ for all samples) and provided robust and comparable parameters across samples. Six parameters were derived: initial intensity (Y_0), plateau, rate constant (K), time

constant ($\tau = 1/K$), half-life ($\ln 2/K$), and span (Y_0 – plateau).

Zebrafish Maintenance

All zebrafish procedures were approved by the Animal Ethics Committee of Changchun University of Chinese Medicine (Approval No. 2024692) and conducted in accordance with zebrafish model organism database (zfin.org) standards. Wild-type AB strain larvae were used. Zebrafish larvae were maintained in an incubator at 28.5 °C with a 14:10 h light/dark photoperiod in embryo medium. For the evaluation experiments described in this research, allocation of larvae to different treatment groups was performed using a completely randomized design generated by random number tables. To minimize observer bias, all subsequent phenotypic assessments were performed by an experimenter who was blinded to the group allocation. The coding of samples was revealed only after data acquisition was complete. For imaging procedures, larvae were anesthetized by immersion in 0.016% tricaine methanesulfonate (MS-222, buffered to pH 7.0) until loss of equilibrium and cessation of voluntary movement. At the end of the experiments, larvae were euthanized by an overdose of MS-222 (0.1%, 10 min) followed by rapid freezing at -80 °C for subsequent biochemical assays, or were immediately processed for RNA extraction as described below.

Safety Assessment (LC_{50} Determination)

LC_{50} assay: At 3 days post-fertilization (dpf), healthy larvae were distributed into 6-well plates (30 larvae per group). Based on preliminary range-finding experiments, CGT extracts were tested at 10, 20, 50, 100, and 200 μg/mL in zebrafish embryo medium, while CGO extracts were tested at 40, 80, 120, 160, and 200 μg/mL. Exposure continued for 144 h, with medium renewal every 24 h. Mortality and morphological abnormalities were recorded daily. The median lethal concentration (LC_{50}) at 144 h was calculated by nonlinear regression (log[inhibitor] vs. normalized response) using GraphPad Prism 10. The non-toxic concentration was defined as the highest concentration causing no mortality or visible abnormalities, and was used to select doses for subsequent efficacy experiments.

MASLD Model Induction and Efficacy Evaluation in Zebrafish

A high-cholesterol diet (HCD)-induced MASLD model was established following a published protocol[44]. Wild-type AB, Tg(mpx:eGFP) (neutrophil reporter), and Tg(mpeg:mCherry) (macrophage reporter) larvae were used.

Diet preparation: The base diet (Larval-AP100, Shanghai Haishengcheng Bio) was mixed with cholesterol dissolved in anhydrous ether to achieve a final concentration of 5% (w/w) cholesterol.

The mixture was stirred thoroughly, and ether was evaporated overnight. The normal diet (ND) was prepared identically without cholesterol.

Treatment regimen: At 5 dpf, larvae were randomly assigned to nine groups: ND control, HCD model, positive control (10 μM Bezafibrate, BZT), and three dose groups each for CGT and CGO extracts. Based on LC_{50} results, the following concentrations were used: CGT at 5, 10, and 20 μg/mL; CGO at 5, 10, and 20 μg/mL. From 5 to 11 dpf, all groups except ND control were fed a high-cholesterol diet (HCD, 2 mg/day, divided into two feedings). Immediately after each feeding, the medium was replaced with fresh solution containing the respective extract or BZT. Larvae were fasted for 12 h before sampling at 11 dpf (Figure 1).

Two independent cohorts of larvae were used for different endpoint analyses. For individual-based phenotypic assessments (Oil Red O staining, ROS fluorescence imaging, neutrophil/macrophage quantification), each group initially contained 30 larvae. Due to natural attrition during the 6-day experimental period, the final number of larvae available for analysis ranged from 15 to 25 per group. For biochemical assays, at 11 dpf, larvae from each group were randomly divided into three pools (30 larvae per pool), with each pool serving as one biological replicate, and the mean of the replicates was used for subsequent statistical analysis.

Lipid accumulation assessment: Larvae were fixed and stained with Oil Red O (Yuanye Bio-Technology) to visualize neutral lipids. Hepatic steatosis was quantified by analyzing staining area and intensity using ImageJ. Whole-larva triglycerides (TG) and total cholesterol (TC) were measured using commercial ELISA kits (Wuhan Enzyme Immunity Biotechnology Co., Ltd.) according to the manufacturer's protocols.

Oxidative stress assessment: Intracellular reactive oxygen species (ROS) levels were measured in live larvae incubated with DCFH-DA probe (BIOFOUNT, Beijing, China). Fluorescence was quantified using ImageJ. Activities of superoxide dismutase (SOD), glutathione peroxidase (GSH-Px), and malondialdehyde (MDA) levels in larval homogenates were determined using ELISA kits (Wuhan Enzyme Immunity Biotechnology Co., Ltd.).

Inflammatory response assessment: Tg(mpx:eGFP) and Tg(mpeg:mCherry) larvae were processed through the same regimen. At 11 dpf, larvae were anesthetized, and the recruitment of neutrophils (GFP^+) and macrophages ($mCherry^+$) to the liver region was visualized and quantified using fluorescence microscopy and ImageJ.

Gene Expression Analysis by Quantitative Real-Time PCR

Total RNA was extracted from 30 pooled larvae per group using TRIzol reagent (Thermo Fisher

Scientific)[45]. RNA concentration and purity were determined spectrophotometrically (CLARIOstar, BMG LABTECH). First-strand cDNA was synthesized from 2 μg total RNA using a reverse transcription kit (Tiangen, China). Quantitative real-time PCR (RT-PCR) was performed using SYBR Green Master Mix (Tiangen) on a CFX96 Deep Well Dx system (Bio-Rad). Each reaction was run in triplicate. Relative expression levels of target genes (cpt1a, fasn, hmger, nrf2, keap1, cat, sod1, gpx1a, tnf-α, il-6) were calculated using the $2^{-\Delta\Delta CT}$ method, with β-actin as the internal control. Primer sequences are listed in Table 1.

Naringin-Normalized Dose-Response Analysis

To account for the significant difference in naringin content between CGT and CGO extracts and to rigorously assess their functional equivalence, we performed a dose-normalized regression analysis integrating data from biochemical assays (Section 2.6) and gene expression analyses (Section 2.7). All crude extract doses were converted to naringin-equivalent concentrations based on the quantified naringin content of each batch (Section 2.2). For each endpoint—including lipid parameters (TC, TG), oxidative stress markers (SOD, GSH-Px, MDA), and relative mRNA levels of key genes (cpt1a, fasn, hmger, nrf2, keap1, cat, sod1, gpx1a, tnf-α, il-6)—data were plotted against naringin-equivalent concentration, and linear regression was performed using GraphPad Prism 10.

To test whether the two varieties differed in their dose-response relationships, analysis of covariance (ANCOVA) was conducted with naringin-equivalent concentration as the covariate and variety (CGT vs. CGO) as the fixed factor. A non-significant variety effect ($p>0.05$) was interpreted as evidence of functional equivalence for that endpoint, provided that the regression slopes were significant and in the expected direction. This approach allowed us to dissect whether the observed phenotypic similarities arose from comparable bioactivity per unit of the primary marker compound or from distinct synergistic interactions within the complex extract matrix.

Statistical Analysis

Multivariate analysis: For metabolomics data, principal component analysis (PCA) was performed to visualize overall metabolite profile differences. Differential metabolites were identified using thresholds of |Fold Change| ≥ 0.585 and $p < 0.05$. Hierarchical clustering heatmaps and KEGG pathway enrichment analysis were conducted using MetaBioAnalyst. For DL data, the six kinetic parameters were auto-scaled and subjected to PCA to distinguish sample groups.

Univariate analysis: Data are presented as mean ± SEM. Comparisons between two groups were performed using unpaired two-tailed Student's t-test. Multiple group comparisons were analyzed by one-way ANOVA followed by Tukey's post hoc test for pairwise comparisons. To account for

multiple comparisons, a false discovery rate (FDR) approach was applied where appropriate, with $q < 0.1$ considered significant. All statistical analyses were performed using GraphPad Prism 10, with $p < 0.05$ considered statistically significant unless otherwise specified.

Data Availability

The datasets generated and/or analyzed during the current study are not publicly available due to as they are part of an institutional database for ongoing projects but are available from the corresponding author on reasonable request.

Code Availability

Not applicable

Acknowledgements

This research was supported by the University-College Joint Scientific and Technological Innovation Fund of Guangzhou University of Chinese Medicine (GZYDG2024G07); the Jilin Provincial Development and Reform Commission (No. 2023C028-1); the Pilotscale Selection Project of Colleges and Universities in Changchun City (No.24GXYSZZ10); the Ministry of Human Resources and Social Security of the People's Republic of China high-level talent project (No.030102070; No.030102071).

The authors would like to thank Mr. Zhongfeng Chen, Ms. Mengyu Jian and Guanshu Biotechnology Services (Changchun) Co., Ltd for providing the technical guidance.

Author Contributions

Min He, Mengmeng Sun and Dong Li designed the study. Yuliang Liu, Qizhong Lian , Jianan Wang and Mengmeng Sun conducted experimental work and data analysis. Xianghe Meng provided zebrafish resource. Yuliang Liu and Mengmeng Sun drafted the manuscript. Davron Dekhkonov, Hilola Ahunova and Komiljon Tojibaev contributed to revisions of the manuscript. All authors read and approved the final manuscript.

Competing Interests

Authors declared no conflict of interest.

References

1. Sarangi, P. K., Srivastava, R. K., Sahoo, U. K. & Vivekanand, V. Resource recovery from Pomelo byproducts for zero waste biorefinery and bioeconomic perspectives. *Process Saf. Environ. Prot.* **186**, 1330–1344, https://doi.org/10.1016/j.psep.2024.04.104 (2024).

2. Tocmo, R., Pena-Fronteras, J., Calumba, K. F., Mendoza, M. & Johnson, J. J. Valorization of pomelo (Citrus grandis Osbeck) peel: A review of current utilization, phytochemistry, bioactivities, and mechanisms of action. *Compr Rev Food Sci Food Saf* **19**, 1969–2012, https://doi.org/10.1111/1541-4337.12561 (2020).
3. Rinella, M. E. & Sookoian, S. From NAFLD to MASLD: updated naming and diagnosis criteria for fatty liver disease. *J. Lipid Res.* **65**, 100485, https://doi.org/10.1016/j.jlr.2023.100485 (2024).
4. Geng, Y., Faber, K. N., de Meijer, V. E., Blokzijl, H. & Moshage, H. How does hepatic lipid accumulation lead to lipotoxicity in non-alcoholic fatty liver disease? *Hepatol Int* **15**, 21–35, https://doi.org/10.1007/s12072-020-10121-2 (2021).
5. El-Sehrawy, A. *et al.* Combating oxidative stress in non-alcoholic fatty liver disease: From mechanisms to therapeutic strategies. *Pathol Res Pract* **272**, 156053, https://doi.org/10.1016/j.prp.2025.156053 (2025).
6. Oladipupo, S. O., Ezenabor, E. H., Ojo, A. B., Ogunlakin, A. D. & Ojo, O. A. Interplay of the pathophysiological mechanisms of non-alcoholic fatty liver disease, diabetes mellitus, and inflammation: A growing threat to public health. *Obes. Med.* 100613, https://doi.org/10.1016/j.obmed.2025.100613 (2025).
7. Ghosh, D. *et al.* Phytotherapy for non-alcoholic fatty liver disease: A review of mechanisms, efficacy, and future directions. *Nat. Ther. Adv.* **8**, 6, https://doi.org/10.53388/NTA2025006 (2025).
8. Miryan, M., Azizi, A., Pasdar, Y. & Moradi, M. Adherence to plant based diets reduce the risk of hepatic fibrosis in nonalcoholic fatty liver disease. *Sci Rep* **15**, 17403, https://doi.org/10.1038/s41598-025-02613-8 (2025).
9. Feng, Q. *et al.* Discovery of pharmacological effects and targets of Citri Grandis Exocarpium based on SYSTCM and virtual screening. *Food Nutr Res* **68**, 10.29219, https://doi.org/10.29219/fnr.v68.10618 (2024).
10. Deng, G. *et al.* Exocarpium Citri Grandis alleviates the aggravation of NAFLD by mitigating lipid accumulation and iron metabolism disorders. *J Ethnopharmacol* **313**, 116559, https://doi.org/10.1016/j.jep.2023.116559 (2023).
11. Hu, M., Zhang, L., Ruan, Z., Han, P. & Yu, Y. The regulatory effects of citrus peel powder on liver metabolites and gut flora in mice with non-alcoholic fatty liver disease (NAFLD). *Foods* **10**, 3022, https://doi.org/10.3390/foods10123022 (2021).
12. Tian, D. *et al.* Coumarin analogues from the *Citrus grandis* (L.) Osbeck and their hepatoprotective activity. *J. Agric. Food. Chem.* **67**, 1937–1947, https://doi.org/10.1021/acs.jafc.8b06489 (2019).
13. Li, Y. J. *et al.* Exocarpium Citri Grandis ameliorates alcoholic liver disease by modulation of hepatic lipid metabolism and iron homeostasis. *Chin Med* **20**, 174, https://doi.org/10.1186/s13020-025-01229-4 (2025).
14. Xian, L. *et al.* The draft genome and multi-omics analyses reveal new insights into geo-herbalism properties of Citrus grandis 'Tomentosa'. *Plant Sci* **325**, 111489, https://doi.org/10.1016/j.plantsci.2022.111489 (2022).
15. Liu, G. *et al.* Sequential grade evaluation method exploration of Exocarpium Citri Grandis (Huajuhong) decoction pieces based on "network prediction --> grading quantization --> efficacy validation". *J Ethnopharmacol* **291**, 115149, https://doi.org/10.1016/j.jep.2022.115149 (2022).

16. Huang, H. *et al.* Evaluation of the authenticity of Citri Grandis Exocarpium based on metabolomics and transcriptomics. *Medicinal Plant Biol.* **4,** 1, https://doi.org/10.48130/mpb-0024-0033 (2024).
17. Su, W.-W. *et al.* The potential application of the traditional Chinese herb Exocarpium Citri grandis in the prevention and treatment of COVID-19. *Tradit. Med. Res.* **5**, 160–166, https://doi.org/10.12032/TMR20200406172 (2020).
18. Hu, S. *et al.* Analysis of volatile compounds in *Citri grandis* from different regions in South China and the response of volatile compounds to ecological factors. *Molecules* **30**, 622, https://doi.org/10.3390/molecules30030622 (2025).
19. Fan, R., Zhu, C., Qiu, D. & Zeng, J. Comparison of the bioactive chemical components and antioxidant activities in three tissues of six varieties of Citrus grandis 'Tomentosa' fruits. *Int. J. Food Prop.* **22**, 1848–1862, https://doi.org/10.1080/10942912.2019.1683027 (2019).
20. Temirbayeva, D., Ibrayev, N. & Kucherenko, M. Distance dependence of plasmon-enhanced fluorescence and delayed luminescence of molecular planar nanostructures. *J. Lumin.* **243**, 118642, https://doi.org/10.1016/j.jlumin.2021.118642 (2022).
21. Committee, C. P. *Pharmacopoeia of the People's Republic of China*. 2025 Edition edn, (China Medical Science Press, 2025).
22. Popp, F.-A. & Yan, Y. Delayed luminescence of biological systems in terms of coherent states. *Phys. Lett. A* **293**, 93–97, https://doi.org/10.1016/s0375-9601(01)00831-3 (2002).
23. Zhu, J. *et al.* Quality-grade analysis of velvet antler materials using ultra-weak delayed luminescence combined with chemometrics. *Qual. Assur. Saf. Crops Foods* **15**, 1–10, https://doi.org/10.15586/qas.v15i4.1311 (2023).
24. Fu, Y. *et al.* Delayed luminescence: An effective measurement for determining the growth ages of forest cultivated ginseng. *Microchem. J.* **210**, 112921, https://doi.org/10.1016/j.microc.2025.112921 (2025).
25. Sun, Q. *et al.* Investigation of the dynamic alteration in delayed luminescence property and their correlation with ginsenoside over the classical nine-cycle steaming and drying processing of black ginseng. *LWT* **218**, 117474, https://doi.org/10.1016/j.lwt.2025.117474 (2025).
26. Sun, M. *et al.* Delayed luminescence: an experimental protocol for Chinese herbal medicines. *Luminescence* **31**, 1220–1228, https://doi.org/10.1002/bio.3094 (2016).
27. Sun, M. *et al.* Characterization of ginsenoside extracts by delayed luminescence, high-performance liquid chromatography, and bioactivity tests. *Photochem. Photobiol. Sci.* **18**, 1138–1146, https://doi.org/10.1039/c8pp00533h (2019).
28. Wang, L. *et al.* Investigation of processing duration on red ginseng quality utilizing delayed luminescence combined with chemometrics and immunomodulatory assessment. *J. Food Compos. Anal.* **143,** 107655, https://doi.org/10.1016/j.jfca.2025.107655 (2025).
29. Shi, F. *et al.* Dictamnine-induced hepatotoxicity in mice: the role of metabolic activation of furan. *Toxicol. Appl. Pharmacol.* **364,** 68–76, https://doi.org/10.1016/j.taap.2018.12.012 (2019).
30. He, K. *et al.* Inactivation of cytochrome P450 3A4 by bergamottin, a component of grapefruit juice. *Chem. Res. Toxicol.* **11,** 252–259, https://doi.org/ 10.1021/tx970192k. (1998).
31. Liang, Y. *et al.* Bergapten: A review of its pharmacology, pharmacokinetics, and toxicity. *Phytother.*

Res. **35,** 6131–6147, https://doi.org/10.1002/ptr.7221 (2021).

32. Katoch, S. & Patial, V. Zebrafish: An emerging model system to study liver diseases and related drug discovery. *J. Appl. Toxicol.* **41**, 33–51, https://doi.org/10.1002/jat.4031 (2021).
33. Shimizu, N., Shiraishi, H. & Hanada, T. Zebrafish as a useful model system for human liver disease. *Cells* **12**, 2246, https://doi.org/10.3390/cells12182246 (2023).
34. Ko, J. H., Nam, D., Um, J. Y., Jung, S. H. & Ahn, K. S. Bergamottin inhibits adipogenesis in 3T3-L1 cells and weight regulation in diet-induced obese mice. *Am. J. Chin. Med.* **46,** 601–615, https://doi.org/10.1142/S0192415X18500313 (2018).
35. Yazıcı, E., Şahin, E., Alvuroğlu, E., Yuluğ, E. & Menteşe, A. Bergamottin reduces liver damage by suppressing inflammation, endoplasmic reticulum and oxidative stress in cafeteria diet-fed mice. *Food Biosci.* **52,** 102371, https://doi.org/10.1016/j.fbio.2023.102371 (2023).
36. Kim, M. J. *et al.* Hypolipogenic effect of shikimic acid via inhibition of MID1IP1 and phosphorylation of AMPK/ACC. *Int. J. Mol. Sci.* **20,** 582, https://doi.org/10.3390/ijms20030582 (2019).
37. Rives, C. *et al.* Oxidative Stress in NAFLD: Role of nutrients and food contaminants. *Biomolecules* **10**, 1702, https://doi.org/10.3390/biom10121702 (2020).
38. Wang, J. *et al.* Alleviating effect of quercetin on cadmium-induced oxidative damage and apoptosis by activating the Nrf2-keap1 pathway in BRL-3A cells. *Front. Pharmacol.* **13,** 969892, https://doi.org/10.3389/fphar.2022.969892 (2022).
39. Qi, Y. *et al.* Luteolin attenuated cisplatin-induced cardiac dysfunction and oxidative stress via modulation of Keap1/Nrf2 signaling pathway. *Free Radic. Res.* **56,** 209–221, https://doi.org/10.1080/10715762.2022.2067042 (2022).
40. Zhang, J. *et al.* Apigenin protects against renal tubular epithelial cell injury and oxidative stress by high glucose via regulation of NF-E2-related factor 2 (Nrf2) pathway. *Med. Sci. Monit.* **25,** 5280, https://doi.org/10.12659/MSM.915038 (2019).
41. Shwartz, A., Goessling, W. & Yin, C. Macrophages in zebrafish models of liver diseases. *Front. Immuno.l* **10**, 2840, https://doi.org/10.3389/fimmu.2019.02840 (2019).
42. Phung, T. D., Le, T. N. & Phung, A. T. Naringin Extracted from Vietnamese Citrus Maxima Peels: Extraction and Optimization. *Agric. Rev.* **46**, 1–8, https://doi.org/10.18805/ag.RF-379 (2025).
43. Lozada, D. N., Pulicherla, S. R. & Holguin, F. O. Widely targeted metabolomics reveals metabolite diversity in jalapeno and serrano chile peppers (*Capsicum annuum* L.). *Metabolites* **13**, 288, https://doi.org/10.3390/metabo13020288 (2023).
44. Fang, X. *et al.* Puerarin induces macrophage M2 polarization to exert antinonalcoholic steatohepatitis pharmacological activity via the activation of autophagy. *J. Agric. Food. Chem.* **72**, 7187–7202, https://doi.org/10.1021/acs.jafc.3c09601 (2024).
45. Cheng, J. *et al.* Investigation of anti-inflammatory effect of essential oil extracted from Achillea alpina L. through multi-omics analysis in zebrafish tail fin amputation model. *J Ethnopharmacol* **344**, 119519, https://doi.org/10.1016/j.jep.2025.119519 (2025).

Figures

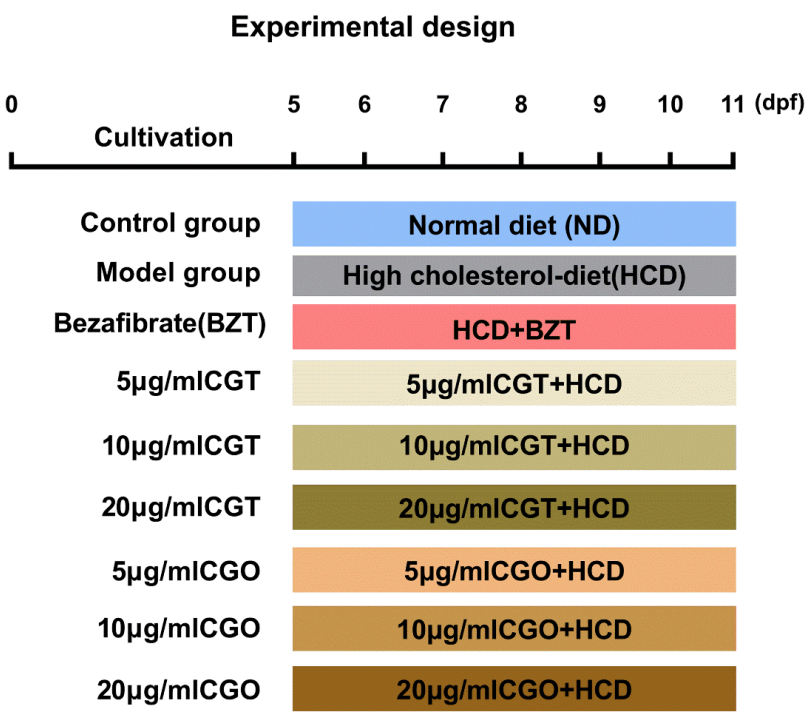

Figure 1. Experimental design for MASLD induction and bioactivity assessment in zebrafish.

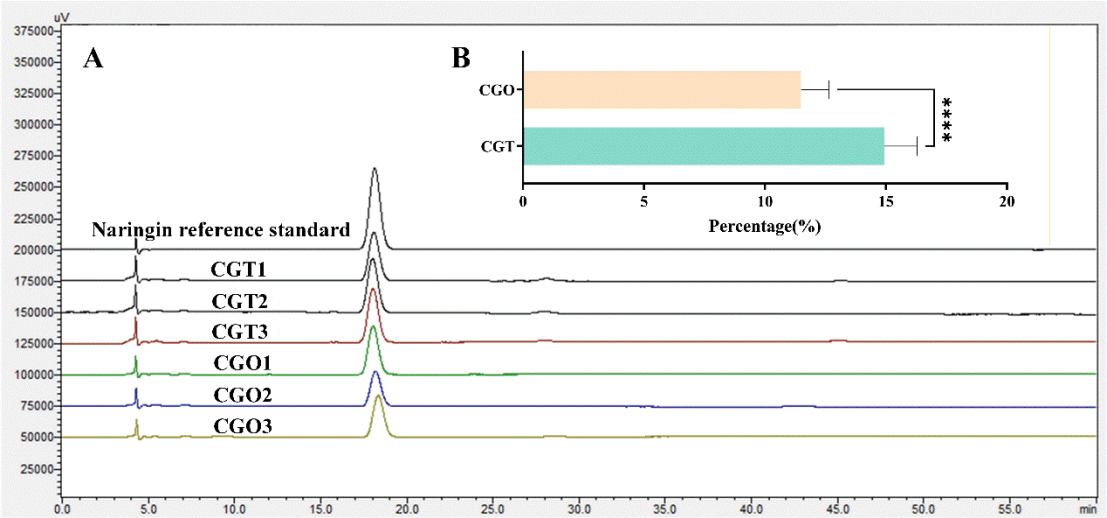

Figure 2. Quantification of naringin in CGT and CGO. (A) Representative HPLC chromatograms. (B) Percentage content of naringin in CGT and CGO. ****p<0.0001.

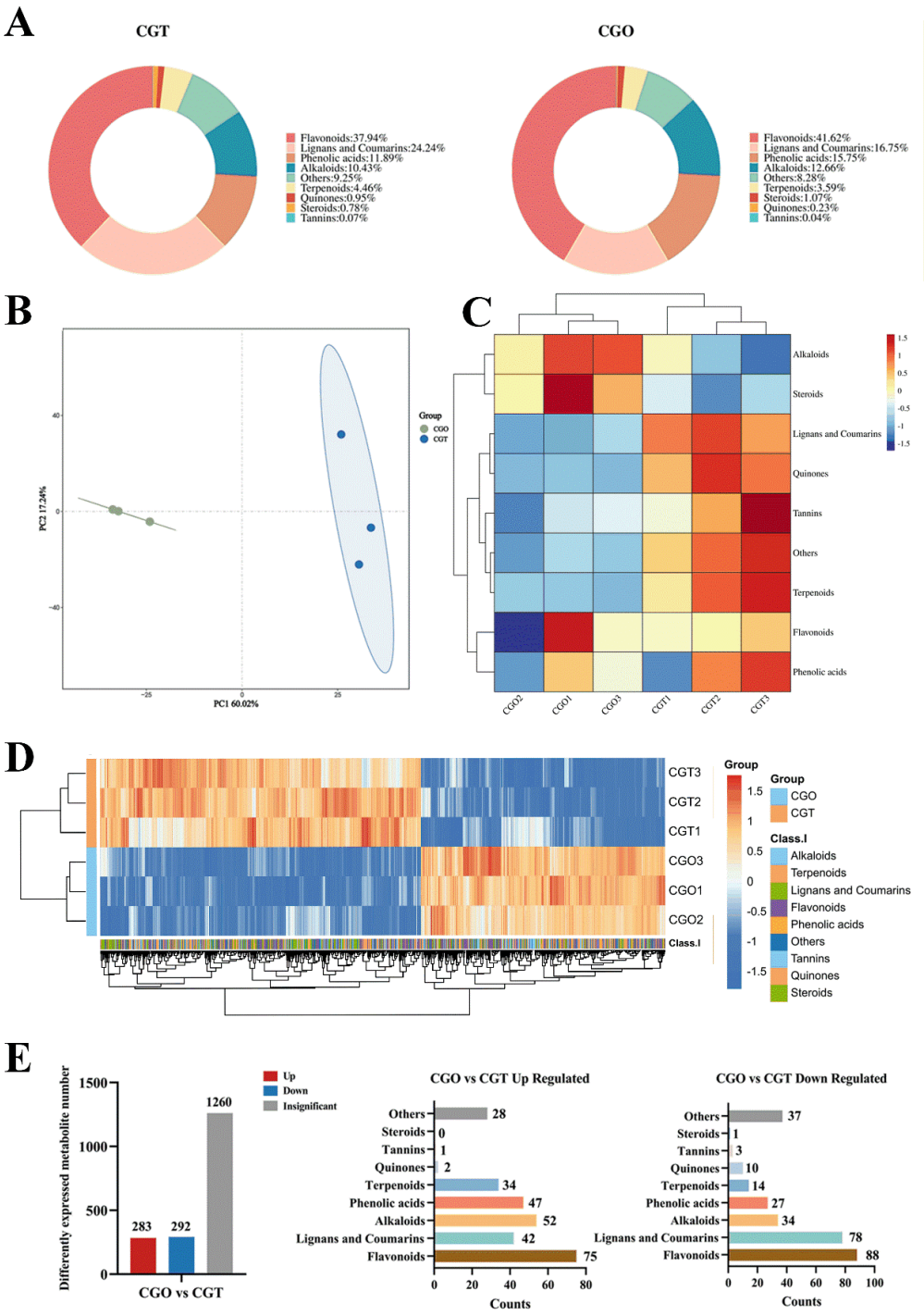

Figure 3. Comparative metabolomics analysis of CGT and CGO. (A) Composition and relative proportion of major metabolite classes detected in CGT and CGO samples. (B) PCA score plot of the metabolomics data, showing distinct clustering of CGT and CGO samples. (C) Heatmap comparing the relative abundance of major metabolite classes between CGT and CGO. (D) Hierarchical clustering heatmap of all detected individual metabolites, illustrating the abundance patterns across CGT and CGO samples. (E) Bar plot showing the number

of significantly upregulated, downregulated, and non-significant metabolites in CGO compared to CGT.

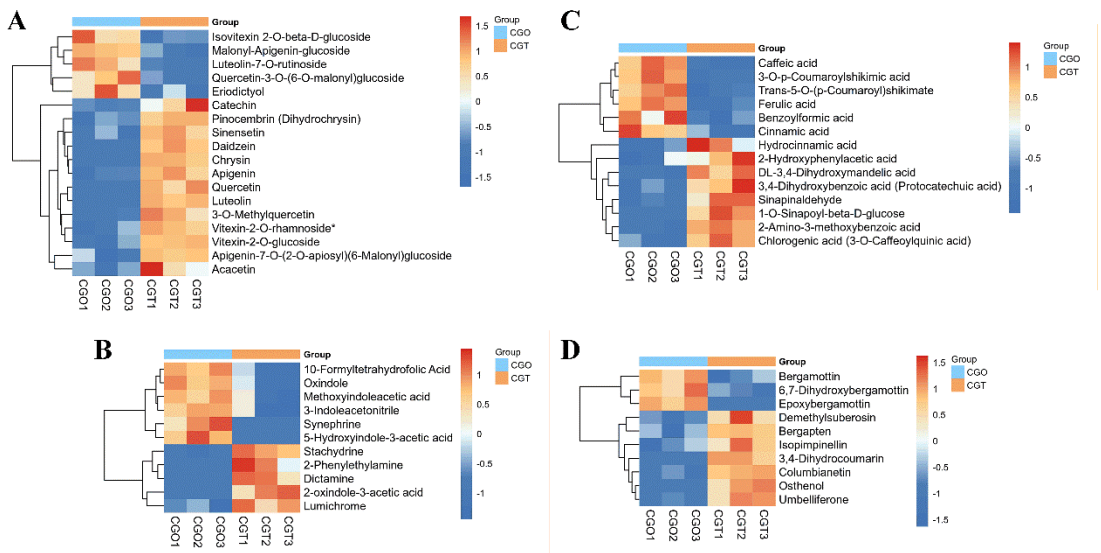

Figure 4. Heatmaps of key differential metabolites within the major classes. (A) Flavonoids. (B) Alkaloids. (C) Phenolic acids. (D) Lignans and coumarins.

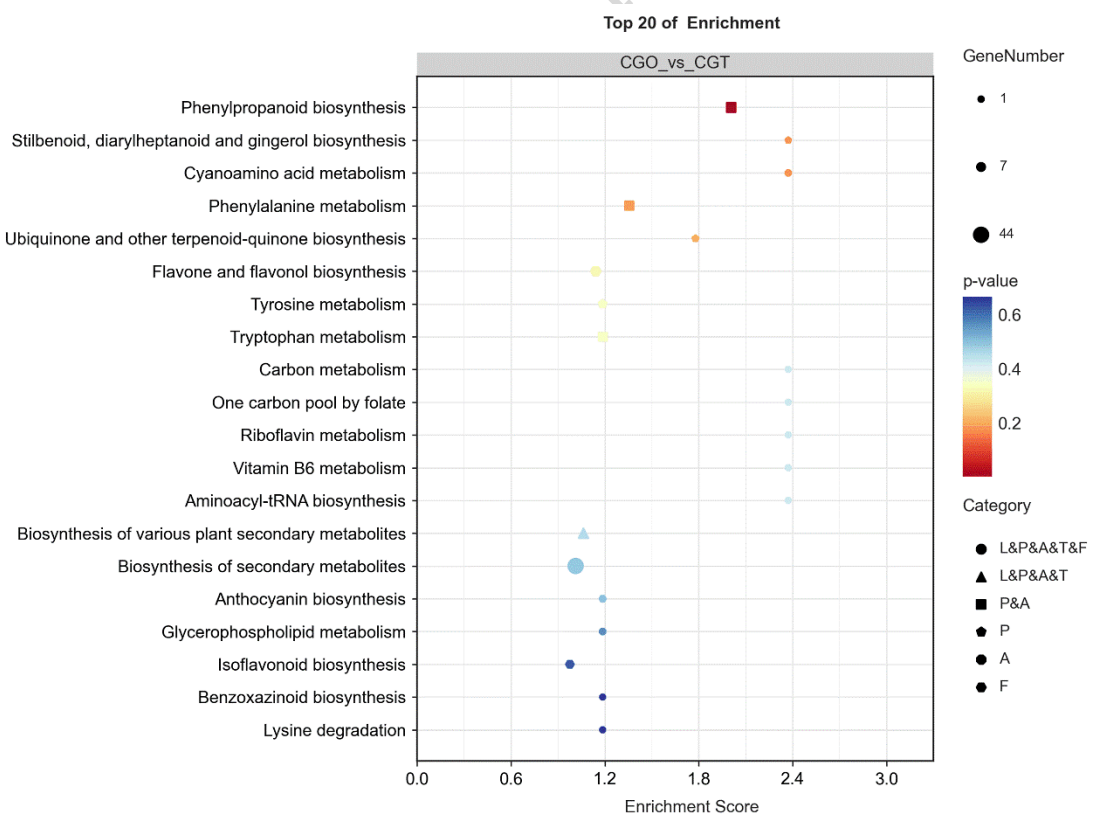

Figure 5. Heatmaps of key differential metabolites within the major classes. F means flavonoids; A means

alkaloids; P means phenolic acids; L means lignans and coumarins; T means terpenoids.

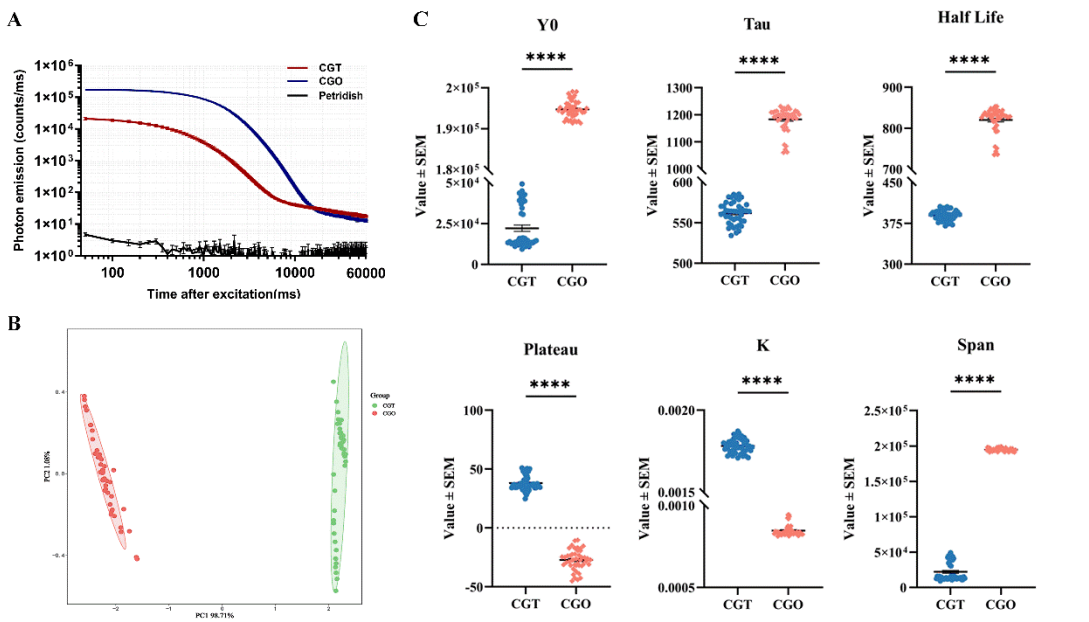

Figure 6. The DL measurement results between CGT and CGO samples. (A) DL decay curves. (B) The PCA scores obtained from the DL data. (C) The six DL parameters analyzed in the samples. Data are presented as mean ± SEM. ****p<0.0001.

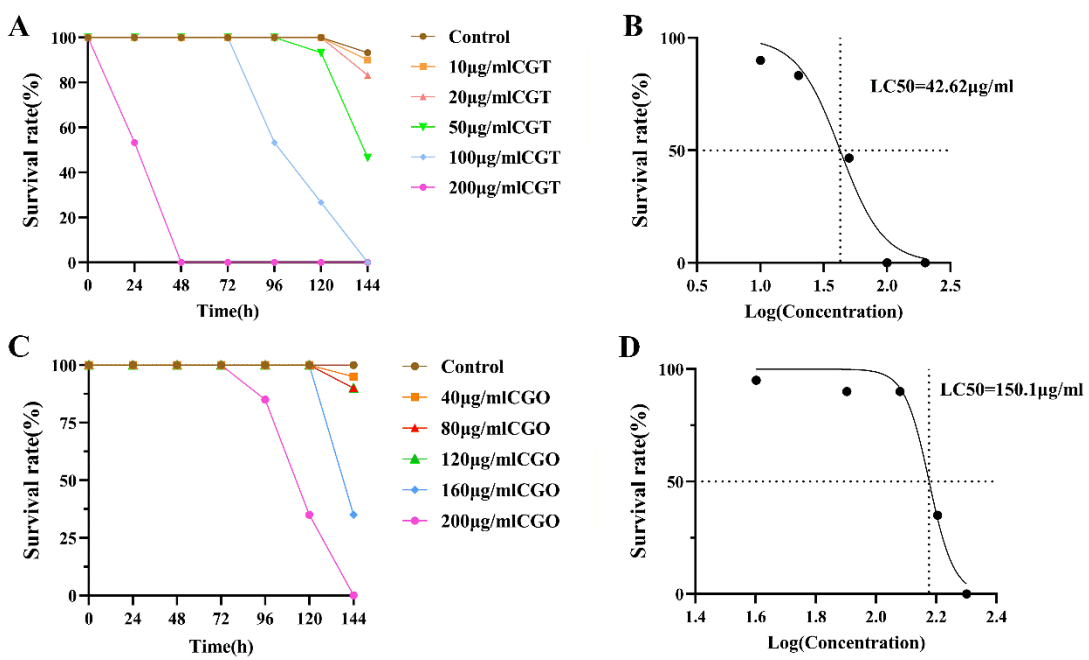

Figure 7. Evaluation of the safety concentration range between CGT and CGO. (A) Survival curves of

larvae exposed to CGT. (B) LC50 of CGT. (C) Survival curves of larvae exposed to CGO. (D) LC50 of CGO.

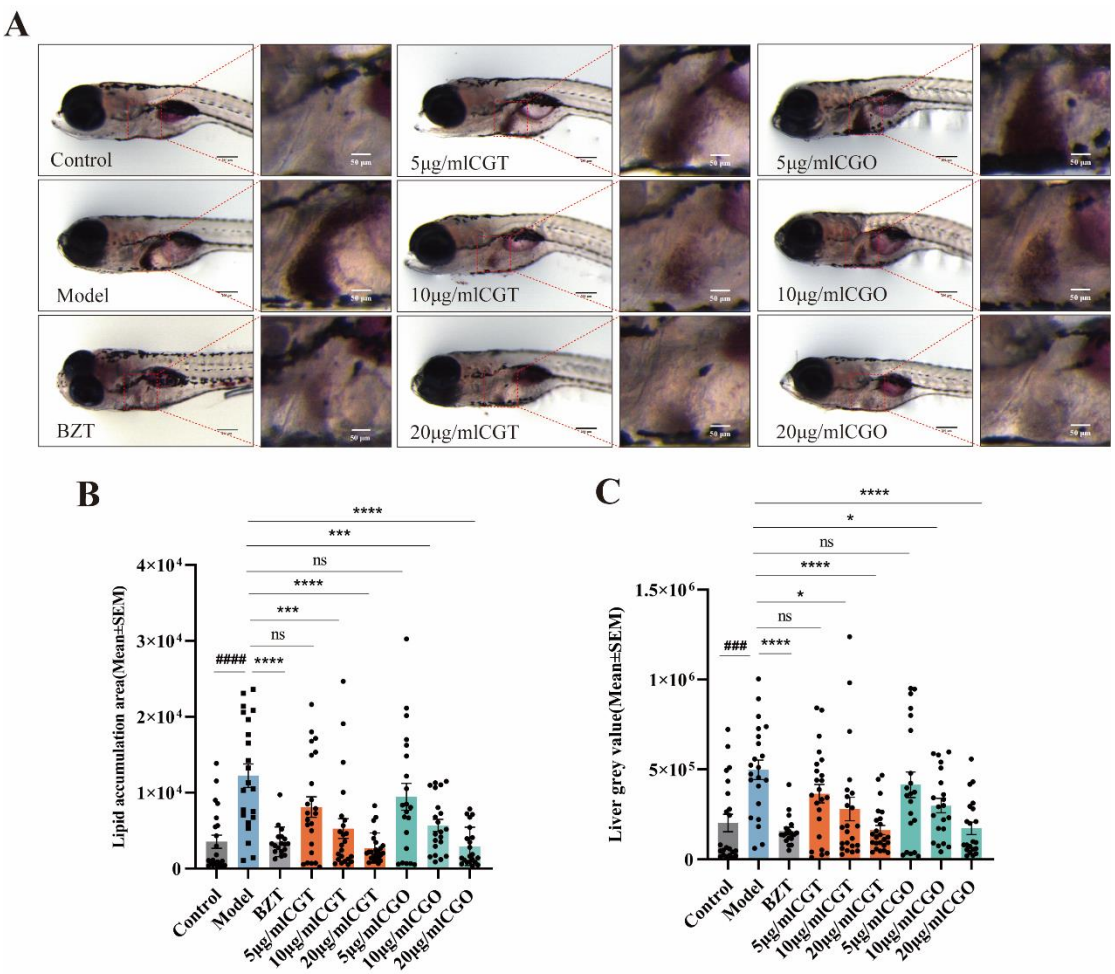

Figure 8. Effects of CGT and CGO extracts on hepatic steatosis in HCD-induced zebrafish. (A) Representative images of Oil Red O staining in zebrafish larvae from different treatment groups. Bar scale (left): 200μm; (right): 50μm. (B, C) Quantitative analysis of hepatic lipid accumulation. (B) Lipid-stained area and (C) staining intensity (grey value) in the liver region were measured. Data are presented as mean ± SEM. *Model versus Treatment, *p<0.05, ***p<0.001, ****p<0.0001; #Control versus Model, ###p<0.001, ####p<0.0001; ns, no significant difference.

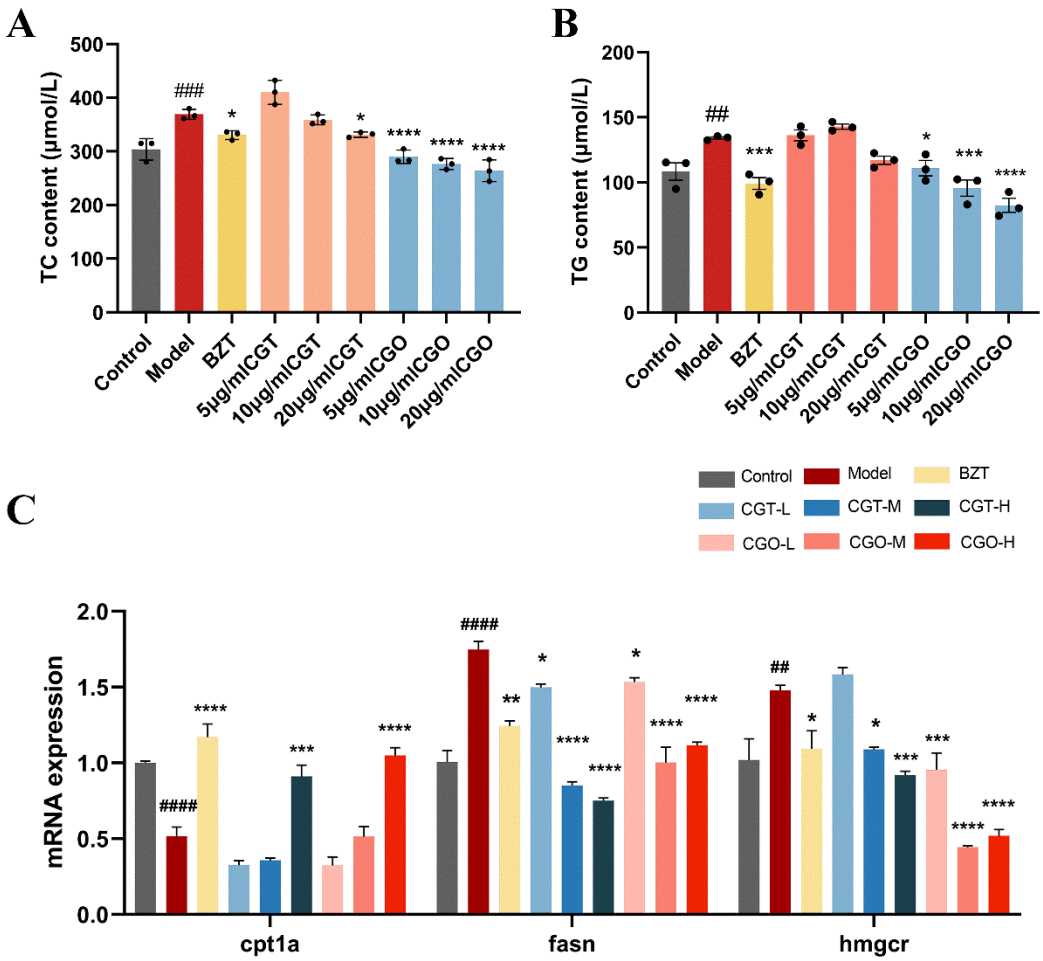

Figure 9. Effects of CGT and CGO extracts on systemic lipid profile and related gene expression. (A, B) Biochemical levels of (A) total cholesterol (TC) and (B) triglycerides (TG) in whole zebrafish larvae. (C) Relative mRNA expression levels of key lipid metabolism genes: cpt1a (fatty acid oxidation), fasn (fatty acid synthesis), and hmgcr (cholesterol synthesis). Gene expression was normalized to *β*-actin and calculated relative to the Control group. Data are presented as mean ± SEM. *Model versus Treatment, *p<0.05, **p<0.01, ***p<0.001, ****p<0.0001; #Control versus Model, ##p<0.01, ###p<0.001, ####p<0.0001. All measurements were performed in triplicate. Doses L, M, and H correspond to concentrations of 5, 10, and 20 μg/mL, respectively.

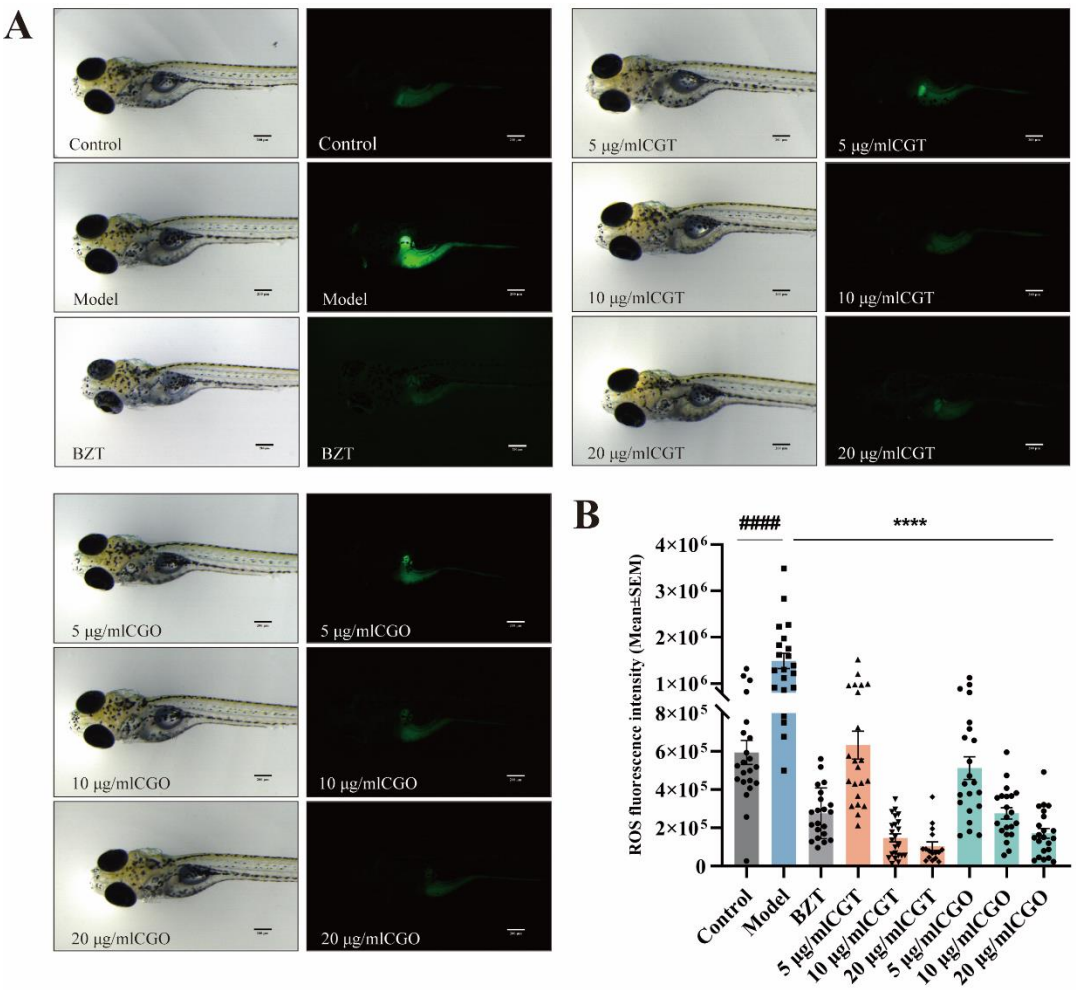

Figure 10. Effects of CGT and CGO extracts on ROS levels in zebrafish larvae. (A) Representative fluorescence images showing ROS levels (green) in the hepatic and intestinal regions of zebrafish larvae detected by the DCFH-DA probe. Bar scale (left): 200μm; (right): 200μm**.** (B) Quantitative analysis of ROS fluorescence intensity. Data are presented as mean ± SEM. *Model versus Treatment, ****p<0.0001; #Control versus Model, ####p<0.0001.

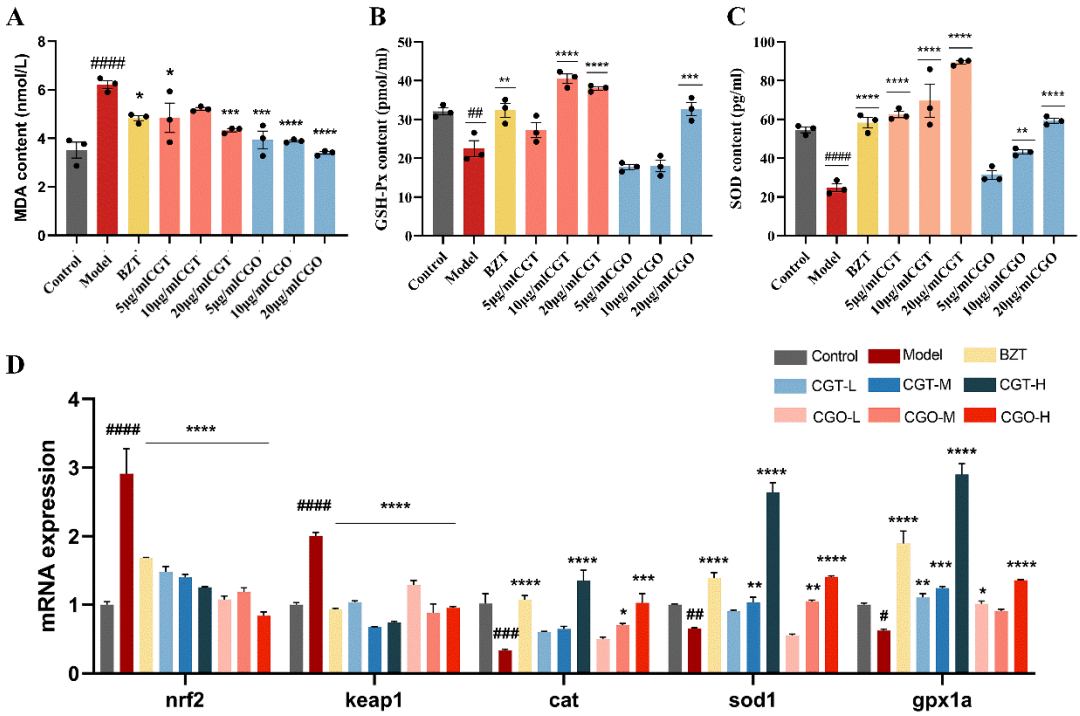

Figure 11. Effects of CGT and CGO extracts on oxidative stress biomarkers and gene expression. (A-C) Biochemical levels of (A) malondialdehyde (MDA), (B) glutathione peroxidase (GSH-Px) activity, and (C) superoxide dismutase (SOD) activity in whole zebrafish larvae. (D) Relative mRNA expression levels of key antioxidant pathway genes: nrf2, keap1, cat, sod1, and gpx1a. Gene expression was normalized to *β*-actin. Data are presented as mean ± SEM. *Model versus Treatment, *p<0.05, **p<0.01, ***p<0.001, ****p<0.0001; #Control versus Model, #p<0.05, ##p<0.01, ###p<0.001, ####p<0.0001. All measurements were performed in triplicate. Doses L, M, and H correspond to concentrations of 5, 10, and 20 μg/mL, respectively.

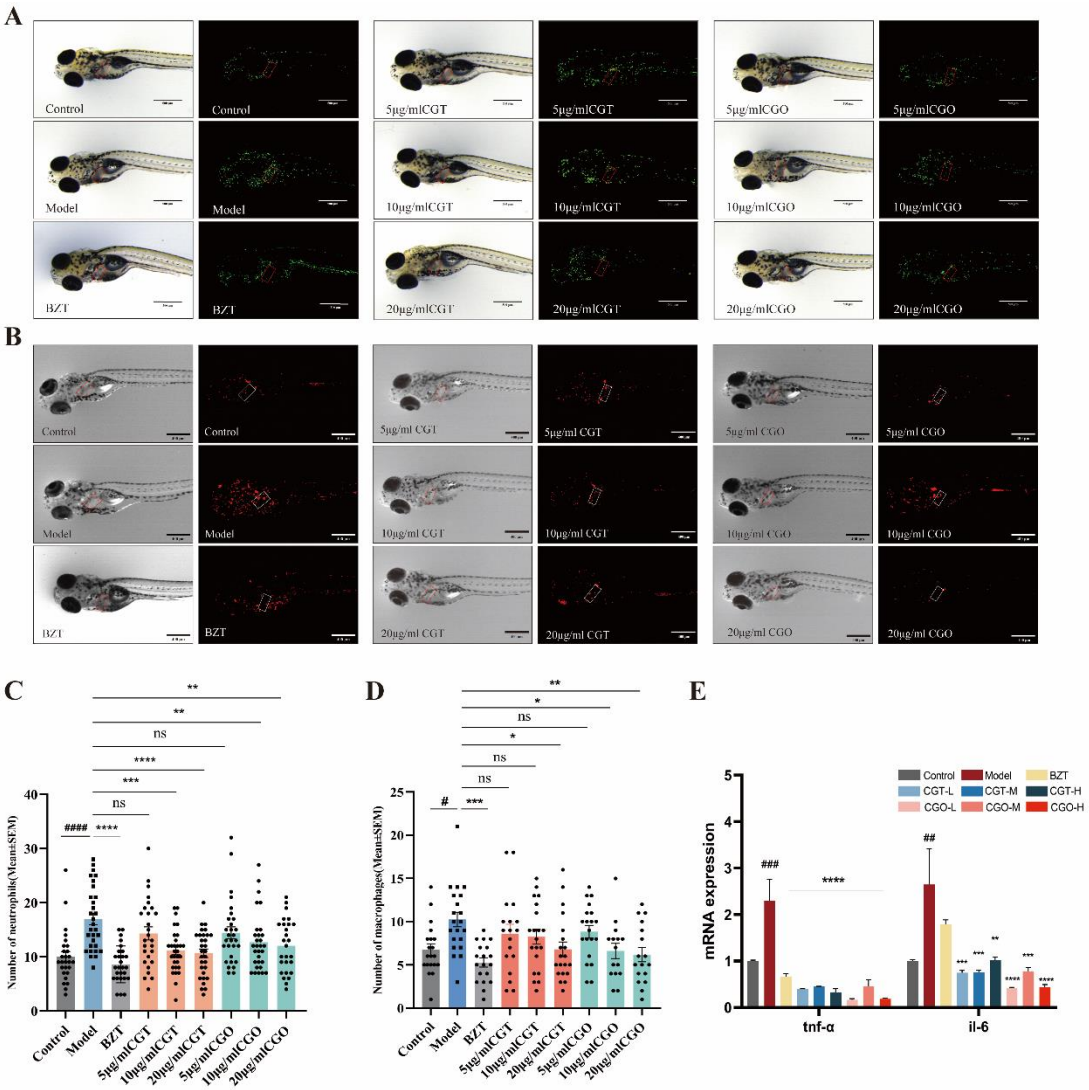

Figure 12. Effects of CGT and CGO extracts on hepatic inflammation in zebrafish larvae. (A, B) Representative fluorescence images showing the recruitment of (A) neutrophils (green, Tg(mpx:eGFP)) and (B) macrophages (red, Tg(mpeg:mCherry)) to the liver region. (C, D) Quantitative analysis of the number of (C) neutrophils and (D) macrophages in the liver region. Data are presented as mean ± SEM. (E) Relative mRNA expression levels of the pro-inflammatory cytokines tnf-α and il-6. Gene expression was normalized to *β*-actin. Data are presented as mean ± SEM. *Model versus Treatment, *p<0.05, **p<0.01, ***p<0.001, ****p<0.0001; #Control versus Model, #p<0.05, ##p<0.01, ###p<0.001, ####p<0.0001. ns, no significant difference. All measurements were performed in triplicate. Doses L, M, and H correspond to concentrations of 5, 10, and 20 μg/mL, respectively.

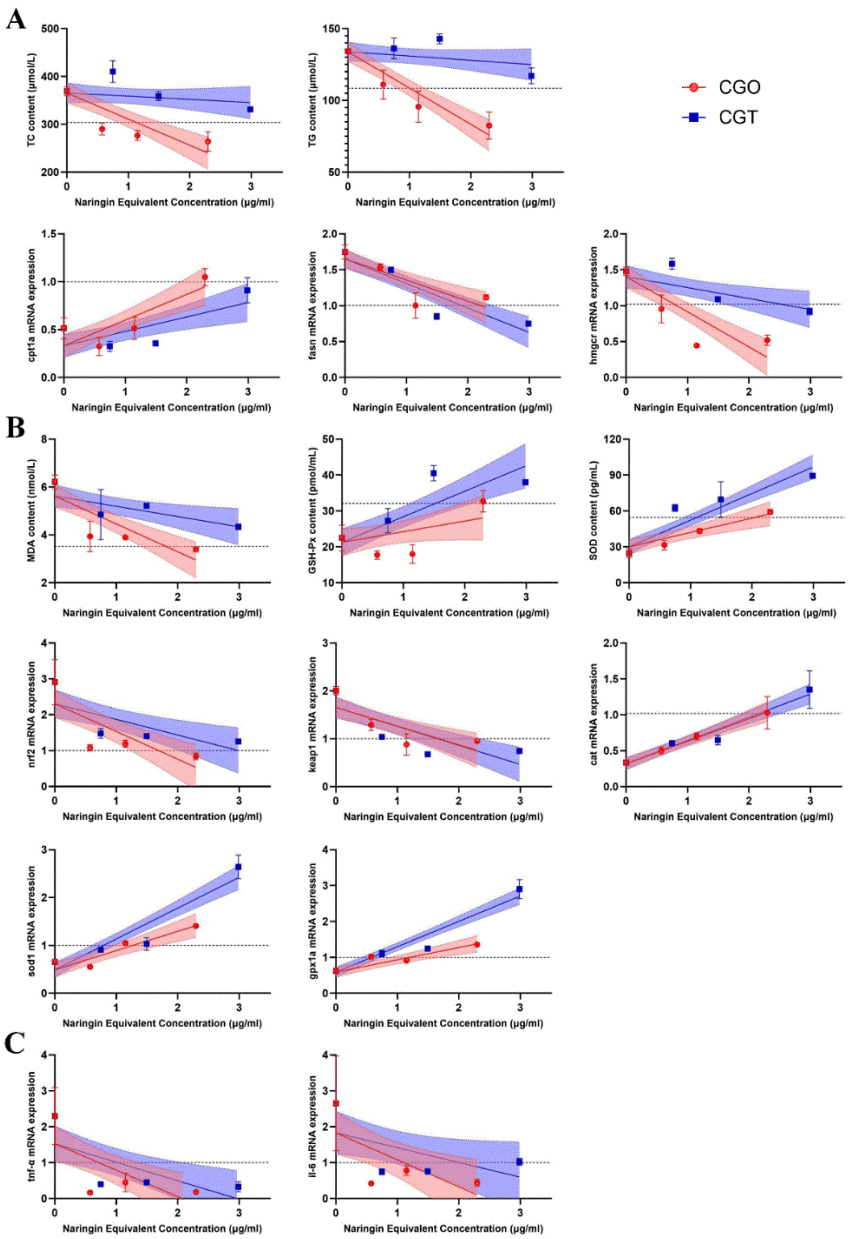

Figure 13. Dose-response regression analysis of biochemical and gene expression markers normalized by Naringin content. (A) Results of hepatic steatosis related biochemical or gene expression levels. (B) Results of oxidative stress related biochemical or gene expression levels. (C) Results of inflammation related gene expression levels. The X-axis represents the Naringin equivalent concentration (μg/mL) converted from crude extract doses. The Y-axis represents the biochemical or gene expression levels. Red lines (CGO) and blue lines (CGT) represent the linear regression fit with 95% confidence bands (shaded areas). The Y-intercept is constrained to the mean of the Model group (shared baseline). The horizontal dashed line represents the mean level of the Control group (target baseline). Note the distinct slopes indicating variety-specific potency in lipid

regulation (e.g., TC, TG) versus antioxidant defense (e.g., SOD).

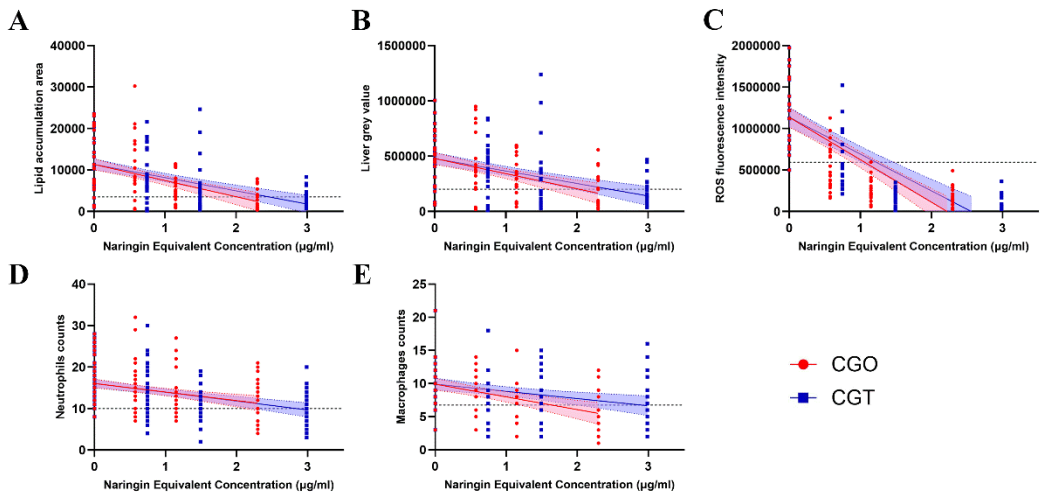

Figure 14. Evaluation of phenotypic bio-equivalence using individual data regression analysis. Scatter plots showing the regression of (A) Lipid accumulation area, (B) Liver grey value, (C) ROS fluorescence intensity, (D) Neutrophils counts, (E) Macrophages counts against Naringin equivalent concentration. Each point represents an individual zebrafish. Red (CGO) and Blue (CGT) areas indicate the 95% confidence bands of the regression lines. The extensive overlap of the confidence bands visually confirms the bio-equivalence of the two varieties at the phenotypic level. The horizontal dashed line indicates the mean of the Control group.

Tables

Table 1. Sequence of primers for the RT-PCR analysis.

Gene	Forward Sequence （5′→3′）	Reverse Sequence （5′→3′）
sod1	ACCGGCACCGTCTATTTCAA	AGCATGGACGTGGAAACCAT
cat	AACTACCAGTCAACTGCCCG	GTCAGGAGCACTGAAGCTGT
gpx1a	TATCATCTGGAGCCCCGTGT	CCTCTTGAATGGTTCCCCGT
il-6	CAGACATCCAGCACTTCCCT	AACAGGATCGAGTGGACCGT
tnf-a	ACCAGGCCTTTTCTTCAGGT	TTTGCCTCCGTAGGATTCAG
nfe2l2a（nrf2)	AGGAGGTGCACCACATTAGG	TCCATGTCCTGTTGGCTTGG
keap1a(keap1)	CCAACGGCATAGAGGTAGTTAT	CCTGTATGTGGTAGGAGGGTT
cpt1a	TGGACCGGGCTCAAATCAAA	ACGTGCTGTACTGAGTCCCT
fasn	GGCCAAAGAGGGAATCACGA	TGATGCTTCAGGGCAGAGTC
hmgcra	GGTGATTGGTGTGGGGACAA	TGGCCAAGACAGACATGCAA
β-actin	GCCAACAGAGAGAAGATGACACAG	CAGGAAGGAAGGCTGGAAGAG

Table 2. ANCOVA results for phenotypic endpoints comparing CGO and CGT efficacy

Endpoint	Difference (CGT – CGO) [95% CI]	*p*-value (Variety)	Interaction *p*-value
Lipid accumulation area	450.3 [-1427 to 2328]	0.6360	0.2637
Liver grey value	16619 [-66734 to 99973]	0.6939	0.3511
ROS fluorescence intensity	52745 [-30980 to 136470]	0.2148	0.6357
Neutrophils count	-0.4862 [-2.097 to 1.124]	0.5520	0.9028
Macrophages count	1.072 [-0.4126 to 2.557]	0.1552	0.5138

The analysis controls for Naringin Equivalent Concentration as a covariate. *P*-values for the “Variety” factor

indicate no significant difference (p>0.05) in therapeutic efficacy between the two groups, supporting the conclusion of equivalence.